RESEARCH

Simple analytical model to use in CAD tools for designing FSS devices: plasmonic transmission through hole arrays in thin films

Nouran M. Ali[1,2] · **Tamer A. Ali**[1,2]

Abstract

Modeling of nano-structured plasmonic surfaces in optical range has attracted great attention in recent research for its various optical properties such as filtering and enhanced transmission of light. In this paper, we present a simple nanocircuit model that can be integrated in CAD tools to design filters and perfect absorbers FSS devices that are based on plasmonic transmission through thin films structured by hole arrays. To illustrate the model potential, we applied it for both circular and square hole arrays on a silver thin film. The model is demonstrated for different structure parameters (hole size and film thickness) in optical frequencies. We show that the model results compare to the numerical calculations obtained from COMSOL Multiphysics software with acceptable deviation and that the model achieves good matching with previously reported experimental measurements.

1 Introduction

Frequency selective surfaces (FSS) are artificial surfaces made of periodically patterned thin metallic layers. Based on the periodicity, FSSs act as frequency filters for selected propagating waves. FSSs are commonly used in frequency-dependent electromagnetic (EM) waves applications, such as filters, perfect absorbers, antenna and radar [1–4]. FSSs can transmit angle- and polarization-independent waves, as it does not rely on surface modes but on a cavity angle-independent mode [5]. Using origami fold/unfold tuning enables transforming single band static FSS to dual band dynamic FSS [6]. This technique increases the degrees of freedom as both symmetric and anti-symmetric modes are excited because of the strong coupling and suitable orientation of the elements.

✉ Nouran M. Ali
eng_nouran@cu.edu.eg

Tamer A. Ali
tali@zewailcity.edu.eg

1 Engineering Mathematics and Physics Department, Cairo University, Faculty of Engineering, Giza 12613, Egypt

2 Communications and Information Engineering Program, University of Science and Technology, Zewail City of Science and Technology, October Gardens, 6th of October, Giza 12578, Egypt

On the other hand, metasurfaces typically have periodicity much smaller than the wavelength, which are designed in terms of average fields and effective macroscopic properties. Also, metasurfaces have an inclusion response as artificial meta-atoms surface [7]. Similarly, Huygens' metasurfaces (HMS) are planar arrays of meta-atom particles of subwavelength size, the array is formed of a balanced electric and magnetic polarizable particles (dipoles), which are defined as an array of Huygens' sources [8]. Based on both electric and magnetic properties, HMS can be designed for many applications such as low or high reflection and antenna beam forming [9]. Like aperture-type FSS, extra-ordinary transmission (EOT) is related to a 2D periodic array of holes in an opaque surface [10]. The transmission from FSS is possible to reach 100% around the resonance frequency of the holes where commonly the hole dimensions are larger than one-half of the period. Unlike the predicted reduction of the transmission with the hole radius, EOT phenomenon appears with very small holes where the design depends on the lattice period rather than the hole radius [11].

Silver (Ag) is one of the most common metals in plasmonic surface design because of its convenient plasmon frequency, high sensitivity, and naturally low ohmic losses at optical frequencies [12]. On the other hand, Ag surfaces applications still face a problem of quick oxidation in many technologies [13].

A theoretical study of EOT through subwavelength hole arrays in optically thick silver films was presented by Martin

et al. [14, 15], where they used thickness = 320 nm ($\approx \lambda$) and the model was applied for square and circular holes. In the long-wavelength limit, the study showed that the transmission coefficient depends on hole area, not shape. Also, in 2011, for thickness = 320 nm, transmission through subwavelength centered-polygonal hole arrays in silver film was numerically investigated, the study observed new hybrid transmission characteristics in octagonal and decagonal hole array [16]. Numerical modeling for nano-structured plasmonic surfaces is regularly performed with different techniques, such as wave concept iterative procedure (WCIP) [17], finite difference time domain (FDTD) [18], finite element method (FEM) [19] and hybrid FDTD/GSM [20, 21]. Numerical approaches are considered more flexible and applicable to wide practical problems compared to analytical models. It can accommodate arbitrary geometries and include a wide range of device physics parameters. That is why it is widely used in FSS modeling studies [22–24].

Although analytical modeling has more limitations than numerical modeling and is not suitable for all frequency ranges and cell dimensions, it is still a sufficient and quick tool to estimate the main parameters and responses. One of the most common analytical methods in designing plasmonic filters is the equivalent circuits. It was used for different shapes in the literature in microwaves frequencies, where the metal is considered as the perfect electrical conductor (PEC) [25–27]. On the other hand, in optical frequencies, metals are no more suitable to be considered as perfect electrical conductors because of the frequency-dependent parameters such as permittivity and conductivity. The equivalent nanocircuit model(ENC) is one of the most common methods which presents a quick and simple way for surface design, but it still has some limitations and deviations than numerical results. Since 2005, Nader Engheta et al. presented some studies in ENC for optical range nano-antennas [28–30]. 1D dielectric/metal/dielectric analytical model in optical frequencies was presented in 2011 [31]. Although circular hole array filters were modeled numerically [23, 24, 32], but up to our knowledge no analytical ENC models were presented for circular holes filter in optical spectrum.

Despite the deviation of ENC results, it still provides fast and easy way to estimate the main characteristics of the transmission spectra compared to the simulation methods and helps reaching better design using optimization techniques. That makes it preferable for FSS applications like filtering , antenna and radar, while doing full-wave simulations is still needed to fine tune the optimized design.

In this work, we present an analytical model that is based on equivalent nanocircuit theory to study circular hole arrays in thin silver plasmonic films. The model is extended for square holes. The model is compared with numerical calculations from COMSOL Multiphysics simulator [33].We used the FEM numerical solver in the simulator to solve the frequency domain form of Maxwell's equations, as FEM is considered a very efficient method to deal with different structures and is convenient to simulate the nano hole array under discussion. The model achieved good matching with published experimental and numerical results.

2 Structure and model

As shown in Fig. 1, the structure contains a silver surface of periodic hole array with radius r, diameter d, periodicity l, and surface thickness t. Using silver parameters from Johnson and Christy [34], the equivalent nanocircuit can be modeled by studying one unit cell due to the symmetry. The model is based on the impedance matching method because of its simplicity and capability to explain fundamental phenomena like extraordinary transmission (EOT)[10, 35].

It is worthy to note that the metal in the optical frequencies has an additional resistance compared to the lower frequencies where the metal is considered as a PEC. So, the impedance in the metal region is dominantly inductive with parallel resistance Z_L, whereas the impedance in the air hole is dominantly capacitive Z_c. As shown in Fig. 2b, Z_c represents the impedance in the circular cavity, whereas, $L_{1,2}$ and $R_{1,2}$ represents the components of the inductance impedance $Z_{1,2}$ in the metallic film.

As shown in Fig. 2a, the inductance impedance in the metal is divided into two parts; Z_{L_1} and Z_{L_2}. Z_{L_2} is estimated approximately from the analogy of the air cavity as a metallic disk removed from the metallic film. So, we used a series equivalent impedance Z_1 and a metallic impedance analogous to the hole impedance Z_2 to calculate Z_{L_2} as follows [36, 37]

$$Z_{L_1} = \frac{jL}{\omega \, \epsilon_0 \, \epsilon_m (L - 2r)t}, \tag{1}$$
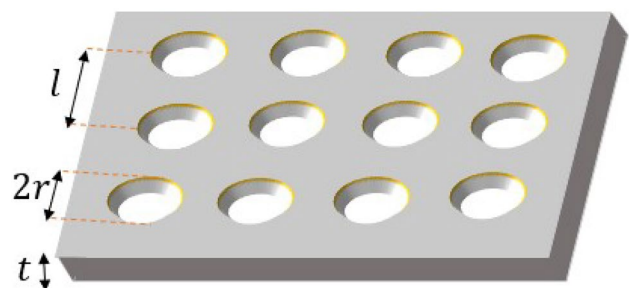
$$Z_{L_2} = Z_1 - Z_2, \tag{2}$$

where

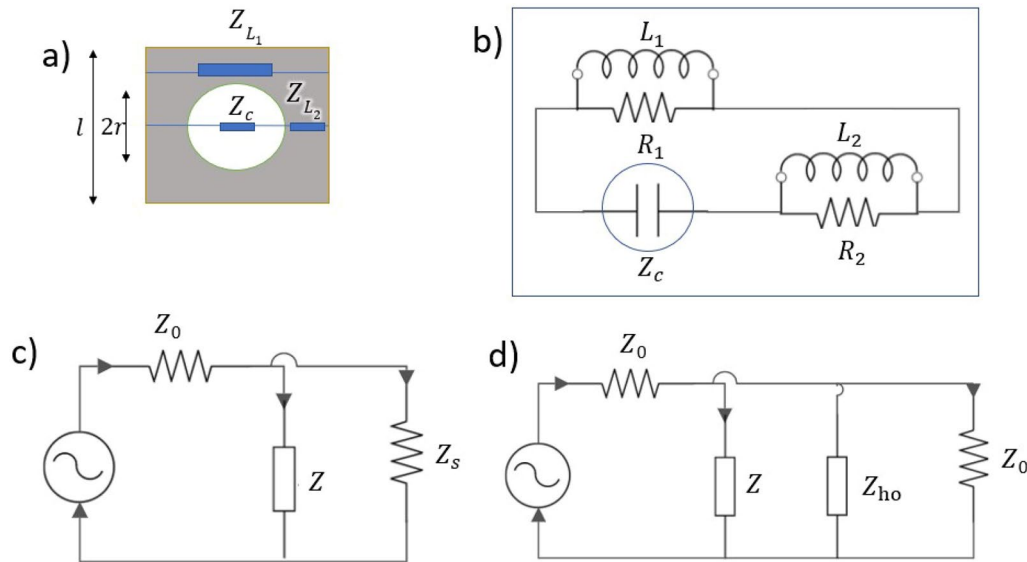**Fig. 1** Schematic of the hole array FSS

Fig. 2 **a** Schematic of the top view of the unit cell, **b** equivalent circuit of the unit cell, **c** the connection of the cell equivalent circuit in with zero-order impedance approximation, **d** the connection of cell equivalent circuit with high-order impedance approximation

$$Z_1 = \frac{jL}{\omega\epsilon_0\epsilon_{\mathrm{m}}(2r)t} \ , \ Z_2 = Z_{\mathrm{c}}/\epsilon_{\mathrm{m}}, \tag{3}$$

$$Z_{L_2} = j\,\frac{4r+L}{\omega\epsilon_0\epsilon_{\mathrm{m}}(2r)t}, \tag{4}$$

where ω is the angular frequency, ϵ_0 is the permittivity of free space, ϵ_{m} is the relative permittivity in the metal.

According to the simplified capacitance formula $C_z = \epsilon_0\epsilon_r\mathrm{Area}/\mathrm{length}$, where, C_z is the capacitance, ϵ_0 is the permittivity of free space, ϵ_r is the dielectric constant and Z is the impedance. The impedance can be estimated as $Z = j/(\omega C_z)$, The same simplified procedure was presented previously for square arrays in the infrared regime [36, 37]

In the circular air hole-filled cavity, as shown in Fig. 3, we divided the area in the capacitance relation into infinitesimally small rods of area $t \times \mathrm{d}y$ and length $2x$ and approximate the capacitance inside the hole $C_{Z_{\mathrm{c}}}$ as follows

$$C_{Z_{\mathrm{c}}} = \int_{-r}^{r} \frac{\epsilon_0 t}{2x}\,\mathrm{d}y, \tag{5}$$

$$C_{Z_{\mathrm{c}}} = \frac{\epsilon_0\,t\,\pi}{2}, \tag{6}$$

$$Z_{\mathrm{c}} = \frac{2j}{\omega\,\epsilon_0\,t\,\pi}. \tag{7}$$

The above approximation is valid for small holes ($d < L/2$), as shown in Fig. 2c, where the zero-order surface
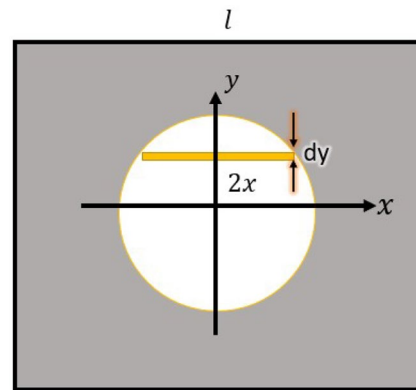

Fig. 3 Circular hole capacitance approximation

impedance approximation ($Z_{\mathrm{S}} = Z_0/\sqrt{\epsilon_r}$) is enough to compensate for the metal loss, where $Z_0 = \sqrt{\mu_0/\epsilon_0}$ is the free space impedance. As the hole radius increases, higher order impedance (Z_{ho}) should be considered, especially the capacitance impedance for TM modes, as shown in Fig. 2d. Both TM and TE frequency-dependent impedance are calculated from circular waveguide approximation as in [38]

$$Z_{TM} = -jZ_0\sqrt{\left(\frac{\lambda}{\lambda_{\mathrm{c}}}\right)^2 - 1}, \tag{8}$$

where λ_{c} is the cutoff wavelength of TM modes (m, n) for a circular waveguide of radius a, $\lambda_{\mathrm{c}} = 2\pi a/\chi_{mn}$, and χ_{mn} is the nth root of mth Bessel function $J_m(\chi)$

On the other hand, TE modes impedance equals

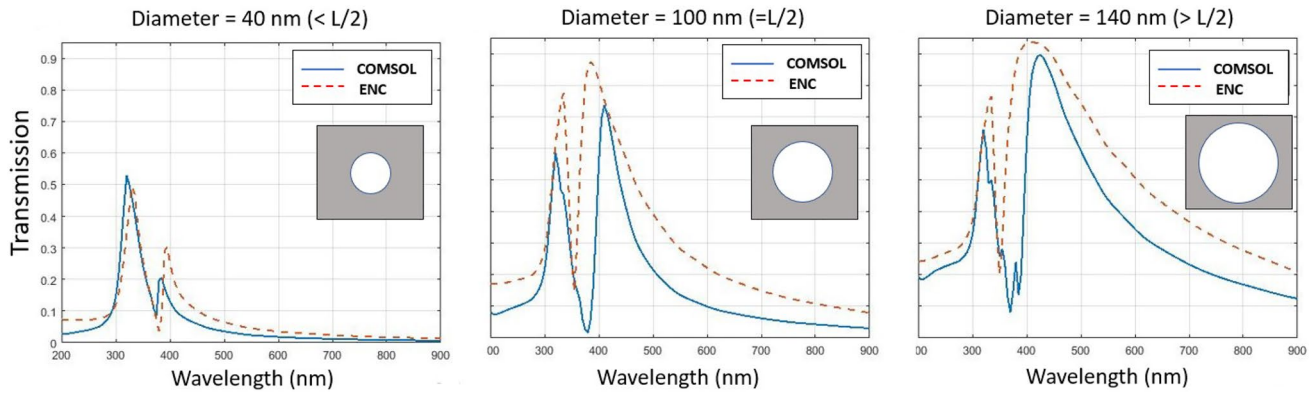**Fig. 4** Transmission for different hole radius: $d = 40$ nm ($d < L/2$), $d = 100$ nm ($d = L/2$), and $d = 140$ nm ($d > L/2$) at $L = 200$ nm and $t = 50$ nm

Table 1 Deviation of ENC model from COMSOL calculations for different radii at $L = 200$ nm and $t = 50$ nm

Deviation	$d = 40$ nm ($d < L/2$)	$d = 100$ nm ($d = L/2$)	$d = 140$nm ($d > L/2$)
D_λ	3.13%	6.1%	3.53%
D_T	6.61 %	18.6%	4.43%

$$Z_{TE} = \frac{jZ_0}{\sqrt{\left(\frac{\lambda}{\lambda_c}\right)^2 - 1}}, \tag{9}$$

where the cutoff wavelength $\lambda_c = 2\pi a / \chi'_{mn}$, and χ'_{mn} is the nth root of mth Bessel function derivative $J'_m(\chi')$.

With the thickness limitation mentioned in Sect. 2.1, field attenuation inside the hole can be neglected and transmission coefficient is calculated from S-parameter $T = |S_{21}|^2$ [36], where

$$S_{21} = S_{11} + 1, \tag{10}$$

$$S_{11} = \frac{Z_{eq} - Z_0}{Z_{eq} + Z_0}, \quad Z_{eq} = \frac{Z_0 Z}{Z_0 + Z}, \tag{11}$$

where Z_{eq} represents the total equivalent impedance (Z) parallel to the free space impedance Z_0.

2.1 The electric nanocircuit model limitations

We are considering the EM problem of insulator–metal–insulator (IMI), where the incident waves are in the z direction (normal to the surface) and E_x is tangent to the surface of the interface. At the interface between the dielectric (with positive real dielectric constant ϵ_2) and the metal (with dielectric function $\epsilon_1(\omega)$), at frequencies below the bulk plasmonic
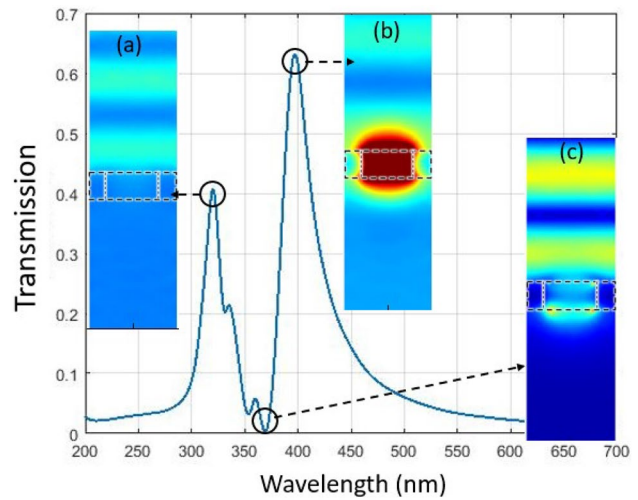

Fig. 5 Transmission spectrum and electric field distribution from numerical simulation at the transmission first peak($\lambda = 320$ nm), dip ($\lambda = 375$ nm) and second peak ($\lambda = 400$ nm) at $L = 200$ nm, $d = 100$ nm and thickness $t = 60$ nm

frequency (ω_p), the dispersion equation of surface plasmon polariton (SPP) propagating at the interface is [39]:

$$\beta = k_0 \sqrt{\frac{\epsilon_1 \epsilon_2}{\epsilon_1 + \epsilon_2}}, \tag{12}$$

where β is the propagation constant of the traveling wave, and $k_0 = \omega/c$ is the wave vector of the wave propagating in vacuum. The non-zero imaginary part of β is associated with attenuation of the surface plasmon, where the energy of the surface plasmon decreases by a factor ($1/e$) at the propagation length ($L_p = 1/(2Im(\beta))$). On the other hand, the propagation constant of the guided modes inside both the metal (γ_m) and the dielectric (γ_d) are calculated as:
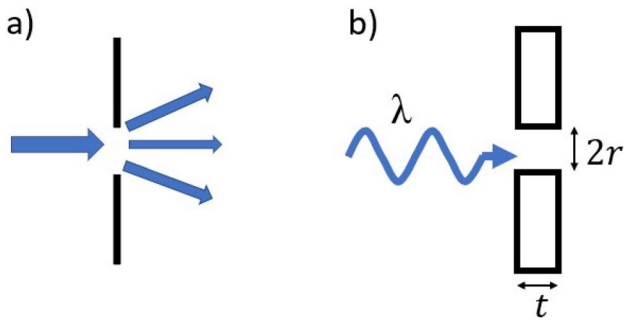
Fig. 6 **a** Diffraction of visible light through a subwavelength hole in an infinitely thin film, **b** the realistic non-zero thickness cylindrical hole with a radius smaller than the wavelength

$$\gamma_m = \frac{-ik\epsilon_m}{\sqrt{(\epsilon_m + \epsilon_d)}} , \ \gamma_d = \frac{ik\epsilon_d}{\sqrt{(\epsilon_m + \epsilon_d)}}. \tag{13}$$

The EM field of the SPP is maximum at the metal–dielectric interface and decays in the direction perpendicular to the interface. The field decreases by a factor of $1/e$ at the penetration depth $l_{p,i} = 1/\mathrm{Re}(\gamma_i)$, where i represents metal or dielectric media [40]. For thick metal films (thicker than penetration depth), the SPP consists of two weakly coupled propagating plasmons on the two surfaces of the metal film. For the above analysis, we propose that the equivalent circuit model is more accurate and valid in thin film plasmonic surfaces (thickness ≤ 100 nm for silver)

Considering the Fabry–Perot resonance [41], the resonance mode (ν_q), at which constructive interference occurs between the incident beam and the circulating beam is at

$$\nu_q = q\Delta\nu_{FSR}, \tag{14}$$

$$\nu_q = \frac{q}{t_{RT}}, \tag{15}$$

where q is the mode index, t_{RT} is the round-trip time, and $\Delta\nu_{FSR}$ is the free spectral range [42]. From the thickness limitation, the first Fabry–Perot resonance mode which occurs approximately at $\nu_1 = 2t/c$, where c represents the speed of light, is out of the frequency range of interest (200–900 nm).

The model can be extended to arbitrary incident angle, the dependence of the impedance on the incident angle is studied in references [43, 44]. for the metallic grid impedance

$$Z_{grid} = Z \times \xi, \tag{16}$$

$$\xi = 1 - k_0^2\sin^2(\theta)/2k_{eff}^2, \tag{17}$$

where $k_{eff} = k_0\sqrt{\epsilon_{eff}}$ is the effective wave number, k_0 is the wave number in free space, and ϵ_{eff} is the effective permittivity. Free space impedance for different incident angle is estimated as follows:

$$Z_{0,TM} = Z_0\cos(\theta), \tag{18}$$

$$Z_{0,TE} = Z_0/\cos(\theta). \tag{19}$$

3 Results

For comparison purposes, we define two figures of merit to demonstrate the relative deviation between the analytical ENC model and numerical results; the peak-wavelength deviation D_λ, at which the maximum transmission takes place, and the transmission deviation D_T, as follows:

$$D_\lambda(\%) = \frac{(|\lambda_{EC} - \lambda_{num}|)}{\lambda_{num}} \times 100\%, \tag{20}$$
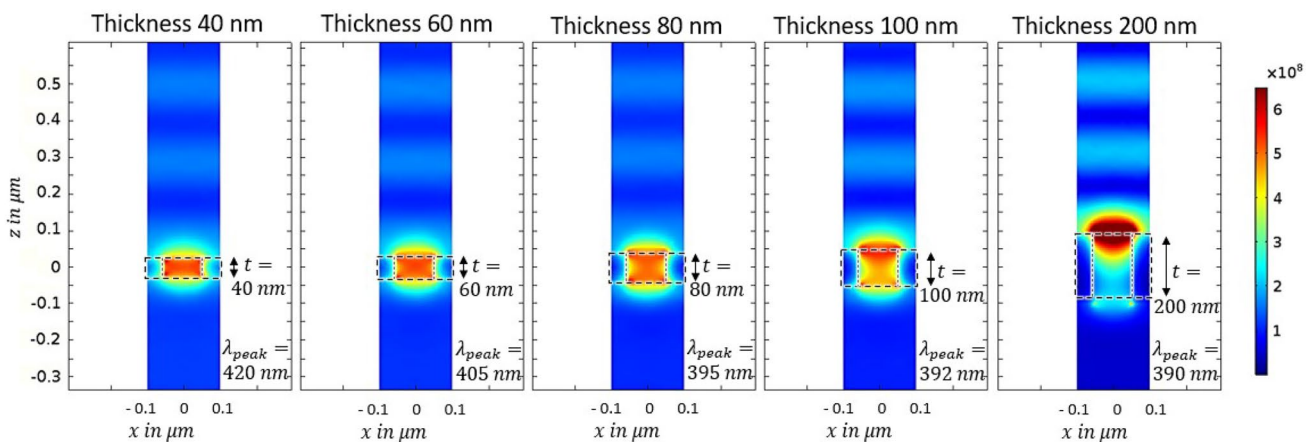

Fig. 7 Electric filed in y–z plane view for different thicknesses from numerical simulation with $d = 100$ nm and $L = 200$ nm, showing the decoupling between SPP at both surfaces at thickness $t > 100$ nm
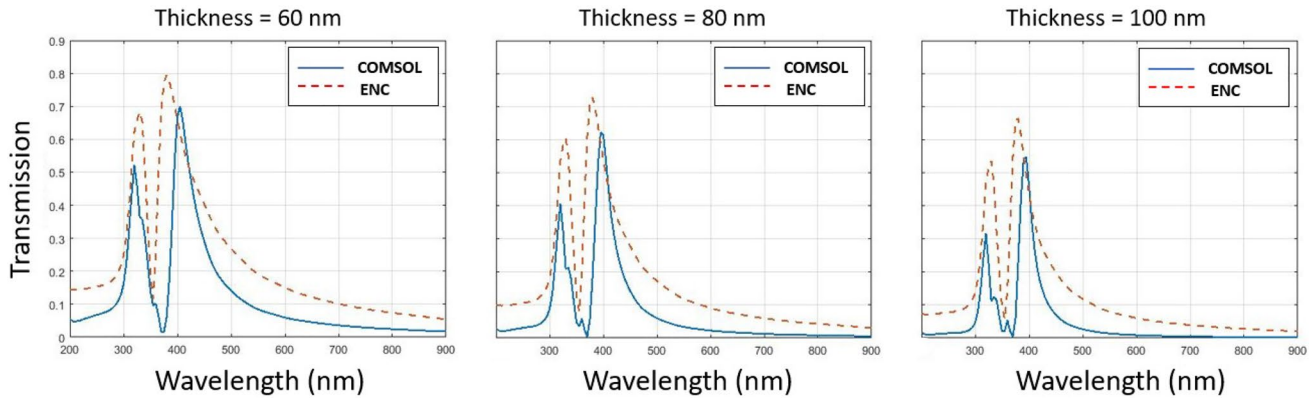
Fig. 8 Transmission for different thickness at diameter 100 nm

Table 2 Deviation of ENC model from COMSOL calculations for different thicknesses at $L = 200$ nm and $d = 100$ nm

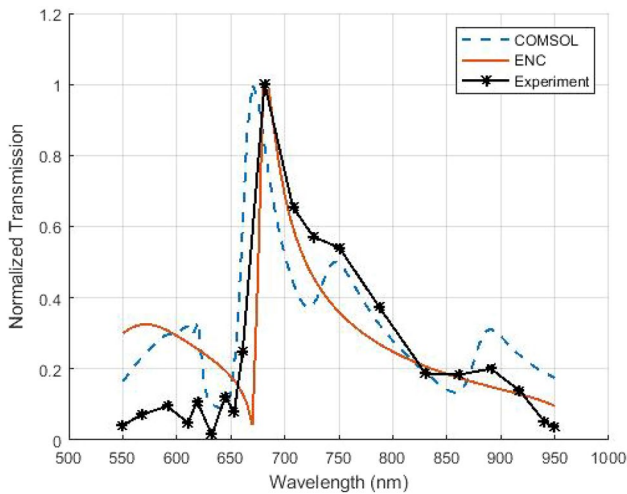| Deviation	$t = 60$ nm	$t = 80$ nm	$t = 100$ nm
D_λ	6.17%	3.8%	3.8%
D_T	13.4%	16.9%	21.18%

Fig. 9 Comparison between experimental [46] measurements, numerical calculations, and ENC results for transmission through surface structured with a hole array

$$D_T (\%) = \frac{(|\, T_{EC} - T_{num}\, |)}{T_{num}} \times 100\%, \qquad (21)$$

where λ_{EC} and λ_{num} are the peak wavelengths of both ENC model results and COMSOL calculations, respectively, and T_{EC} and T_{num} are the maximum transmission of ENC results and COMSOL calculations. The parameters, D_λ and D_T are defined to illustrate the deviation from the numerical study either in the wavelength of the peak or the maximum

transmission value, which are very important in optical filtering application. It is worthy to mention that the deviation in the maximum transmission is not necessarily occurring at the same wavelength .

For comparison, the model is simulated, numerically, by COMSOL Multiphysics Software, which is considered as one of the most suitable tools for simulating different plasmonic structures.

3.1 Hole size effect

As shown in Fig. 4, increasing the hole diameter results in more light transmission. The equivalent nanocircuit achieved good matching for small holes where the diameter is smaller than half the periodicity with only zero-order impedance approximation with a deviation of peak-wavelength and transmission about 3% and 6.6%, respectively, as mentioned in Table 1. On the other hand, ENC of large holes requires additional high-order impedance approximation. Higher-order modes are presented to expand the ENC model in large hole sizes and to reduce the deviation between the model and numerical results. The periodicity and thickness were kept constant ($L = 200$ nm, $t = 50$ nm), where the hole diameter changes with respect to it in three domains: $d = 40$ nm ($d < L/2$), $d = 100$ nm ($d = L/2$), and $d = 140$ nm ($d > L/2$).

3.2 Thickness effect

As shown in the transmission spectrum from numerical simulation, Fig. 5, it has three main features to be examined: first peak at $\lambda = 320$ nm, a dip at $\lambda = 375$ nm, and a second peak at $\lambda = 400$ nm.

For the first peak, increasing the thickness does not affect the wavelength of the peak, as shown in Fig. 8, where the wavelength of the first peak is almost constant at

Fig. 10 **a** Schematic of the top view of the square hole unit cell, **b** equivalent circuit of the unit cell
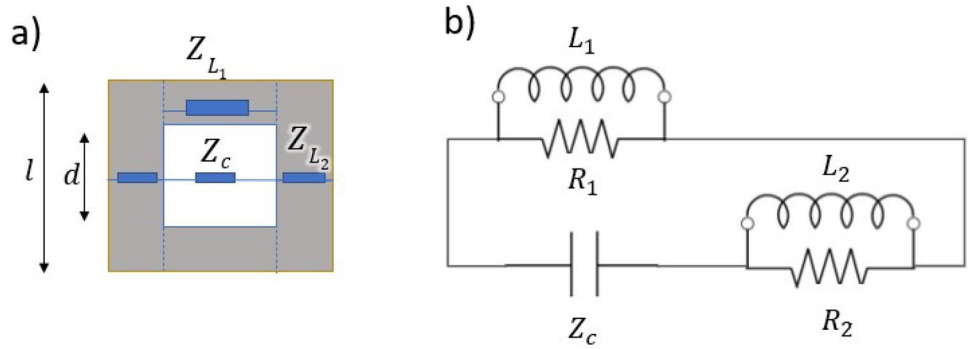
$\lambda = 320$ nm for different thicknesses. This can be explained from the diffraction theory and electric field distribution around the hole edge shown in Fig. 5a.

When light scatters through subwavelength apertures in very thin perfect metal film, it diffracts at the edges, as shown in Fig. 6a, with a transmission related to both hole radius and light wavelength by factor $(r/\lambda)^4$ [45]. However, the transmission in a non-zero thickness hole is characterized by waveguide properties where the transmission is exponentially small above the cutoff wavelength λ_c [11]. Although the cutoff frequency of cylindrical waveguide only depends on the hole radius, the skin depth in real metal increases the cutoff frequency when is taken into account.

On the other hand, the second peak results from SPP where the electric field is concentrated at the hole edge and the EM wave propagates along the surface as shown in

Fig. 5c. The second peak is highly affected by the thickness increase as the coupling between the two surfaces SPP decreases, as shown in Fig. 7. As explained in Sect. 2.1, as the field decays by factor of $1/e$ at the penetration depth inside the metal. That's why decoupling is clear at thickness $t > 100$ nm.

As shown in Fig. 8, comparing the ENC results and COMSOL calculations shows the model sufficiency in estimating both peak-transmission wavelength, and transmission value. The maximum deviation of peak-wavelength is about 6%, whereas the transmission deviation is about 21%, as mentioned in Table 2.

3.3 Comparison with previously reported results

For validation purposes, we compared the proposed ENC model with the experimental measurements reported in [46] for a gold surface structured with a circular hole array (the diameter of the aperture is 200 nm and the periodicity of the array is 600 nm), in which the holes were fabricated through 120 nm thick gold and 80 nm thick silicon nitride layers.

Adjusting the conductivity and structure dimensions values to compensate the actual loss and fabrication
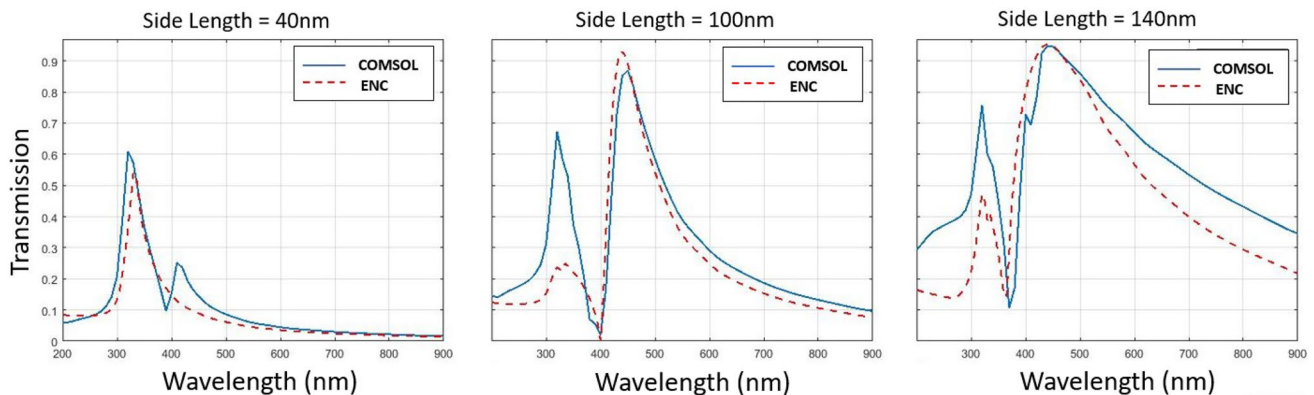
Table 3 Deviation between ENC model results and COMSOL calculations for different side lengths at $L = 200$ nm and $t = 40$ nm

Deviation	$d = 40$ nm $(d < L/2)$	$d = 100$ nm $(d = L/2)$	$d = 140$nm $(d > L/2)$
D_λ	3.13%	2.2%	0%
D_T	11.38%	6.95%	0.71%

Fig. 11 Transmission for different hole side length

varieties in the experimental measurements (as shown in Fig. 9), the ENC results were accurate within 3% of the reported values [46].

As shown in Fig. 9, despite the model is efficient in estimating the main peaks locations, it could not detect the secondary peaks because of the approximations in the analytical model where $d < L/2$ as discussed in Sect. 3.1. This is acceptable for example in designing filters, where a designer is more concerned with the main peaks. So, the model can avoid the long numerical calculation times if used by CAD tools for designing the main features. Once a design is decided on, the designer can do a detailed study or sensitivity analysis in full-wave simulators if needed [47, 48].

4 Model discussion and extension to other cases

In this section, we demonstrate that with suitable impedance representation, ENC modeling can be applied for different hole shapes. In addition to the conventional circular hole shape, other shapes were fabricated such as square[49], rectangle [50] and hexagon [51] hole arrays.

As an example, we apply the ENC model for square hole array shown in Fig. 10. The main modeling procedure is based on representing the metal region with inductance impedance and dielectric regions with capacitance impedance. A previous study of square metal (ITO) plasmonic surface was presented in infrared region with similar procedure [36].

The impedance in both metal and air regions are estimated as follows:

$$Z_c = \frac{j}{\omega \epsilon_0 t}, \tag{22}$$

$$Z_{L_1} = j\frac{d}{\omega \epsilon_0 \epsilon_m (L-d)t}, \tag{23}$$

$$Z_{L_2} = j\frac{L-d}{\omega \epsilon_0 \epsilon_m Lt}. \tag{24}$$

As shown in Table 3, the transmission is estimated for three values of the square hole side length; representing three different domains compared with the periodicity ($< L/2, = L/2, > L/2$). The ENC results achieved good matching with COMSOL calculations especially in estimating the peak-transmission wavelength, as shown in Fig. 11, which increase the reliability of the model in designing filters.

5 Conclusion

We present a simple and efficient theoretical model for hole array in plasmonic silver surface. The model extends the conventional equivalent circuit approach to the optical frequencies where the metal cannot be considered as perfect conductor. Applying the model for circular hole array with different radii and thickness shows the simple model effectiveness in designing FSS with hole arrays for optical applications. The model is compared with experimental measurements and numerical model calculations built by COMSOL Multiphysics and showed an acceptable deviation for an analytical model. The ENC model can be a good basis for designing FSS in CAD tools in the future rather than the need for full-wave simulators.

Declarations

References

1. R.A. Pandhare, F.L. Lohar, C. Dhote, Y. Solunke, Design of FSS based radome wall for airborne radar application. J. Microw. Optoelectron. Electromagn. Appl. **20**, 855–869 (2021)

2. B. Liu, K. Song, J. Xiao, Two-dimensional optical metasurfaces: from plasmons to dielectrics. Adv. Condens. Matter Phys. **2019** (2019)

3. M.F. Nakmouche, A.M. Allam, D.E. Fawzy, D.-B. Lin, Development of a high gain FSS reflector backed monopole antenna using machine learning for 5G applications. Prog. Electromagn. Res. M **105**, 183–194 (2021)

4. A. Ghavidel, M. Kokkonen, S. Myllymäki, A double layer FSS filter for sub-THz applications. Sci. Rep. **11**(1), 1–8 (2021)

5. D. Van Labeke, D. Gérard, B. Guizal, F.I. Baida, L. Li, An angle-independent frequency selective surface in the optical range. Opt. Express **14**(25), 11945–11951 (2006)

6. A. Biswas, C.L. Zekios, S.V. Georgakopoulos, Transforming single-band static FSS to dual-band dynamic FSS using origami. Sci. Rep. **10**(1), 1–12 (2020)

7. S.A.H. Gangaraj, F. Monticone, Molding light with metasurfaces: from far-field to near-field interactions. Nanophotonics **7**(6), 1025–1040 (2018)

8. M. Chen, M. Kim, A.M. Wong, G.V. Eleftheriades, Huygens' metasurfaces from microwaves to optics: a review. Nanophotonics **7**(6), 1207–1231 (2018)

9. A.M. Wong, G.V. Eleftheriades, Perfect anomalous reflection with a bipartite Huygens' metasurface. Phys. Rev. X **8**(1), 011036 (2018)

10. F. Medina, F. Mesa, R. Marqués, D.C. Skigin, Extraordinary transmission as an impedance-matching problem. In: Applications of Metamaterials, pp. 24–1. CRC Press, Boca Raton (2017)

11. T. Ebbesen, C. Genet, Light in tiny holes. Nature **445**(4), 39–46 (2007)

12. S. Goetz, M. Bauch, T. Dimopoulos, S. Trassl, Ultrathin sputter-deposited plasmonic silver nanostructures. Nanoscale Adv. **2**(2), 869–877 (2020)

13. J.K. Bhattarai, M.H.U. Maruf, K.J. Stine, Plasmonic-active nanostructured thin films. Processes **8**(1), 115 (2020)

14. L. Martin-Moreno, F. Garcia-Vidal, H. Lezec, K. Pellerin, T. Thio, J. Pendry, T. Ebbesen, Theory of extraordinary optical transmission through subwavelength hole arrays. Phys. Rev. Lett. **86**(6), 1114 (2001)

15. L. Martin-Moreno, F. Garcia-Vidal, Optical transmission through circular hole arrays in optically thick metal films. Opt. Express **12**(16), 3619–3628 (2004)

16. H.E. Arabi, M. Park, M. Pournoury, K. Oh, Enhanced optical transmission through sub-wavelength centered-polygonal hole arrays in silver thin film on silica substrate. Opt. Express **19**(9), 8514–8525 (2011)

17. A. Sassi, N. Sboui, A. Gharbi, H. Baudrand, Modeling of waveguide filter using wave concept iterative procedure. Circuits Syst. **12**(2), 13–22 (2021)

18. G.D. Smith, G.D. Smith, G.D.S. Smith, *Numerical Solution of Partial Differential Equations: Finite Difference Methods* (Oxford University Press, Oxford, 1985)

19. G. Strang, G.J. Fix, *An Analysis of the Finite Element Method* (Prentice-Hall, Englewood Cliffs, 1973)

20. J. Kim, G. Caire, A.F. Molisch, Quality-aware streaming and scheduling for device-to-device video delivery. IEEE/ACM Trans. Netw. **24**(4), 2319–2331 (2015)

21. K. El Mahgoub, F. Yang, A.Z. Elsherbeni, Analysis of multilayer periodic structures with different periodicities using a hybrid FDTD/GSM method. In: 2011 IEEE MTT-S International Microwave Symposium, pp. 1–4. IEEE (2011)

22. A. Mekawy, M. Khalifa, T.A. Ali, A.H. Badawi, Tuning optical properties of metasurface via piezoelectric effect. IET Optoelectron. **13**(3), 134–138 (2019)

23. D. Kotlarek, S. Fossati, P. Venugopalan, N.G. Quilis, J. Slabỳ, J. Homola, M. Lequeux, F. Amiard, M.L. de la Chapelle, U. Jonas et al., Actuated plasmonic nanohole arrays for sensing and optical spectroscopy applications. Nanoscale **12**(17), 9756–9768 (2020)

24. M. Khammar, Electric field distribution of nanohole thin gold film for plasmonic biosensor: finite element method (2016)

25. A.E. Olk, D.A. Powell, Accurate metasurface synthesis incorporating near-field coupling effects. Phys. Rev. Appl. **11**(6), 064007 (2019)

26. T. Liu, S.-S. Kim, Design of wide-bandwidth electromagnetic wave absorbers using the inductance and capacitance of a square loop-frequency selective surface calculated from an equivalent circuit model. Opt. Commun. **359**, 372–377 (2016)

27. F. Mesa, M. García-Vigueras, F. Medina, R. Rodríguez-Berral, J.R. Mosig, Circuit-model analysis of frequency selective surfaces with scatterers of arbitrary geometry. IEEE Antennas Wirel. Propag. Lett. **14**, 135–138 (2014)

28. A. Alù, A. Salandrino, N. Engheta, Coupling of optical lumped nanocircuit elements and effects of substrates. Opt. Express **15**(21), 13865–13876 (2007)

29. N. Engheta, Circuits with light at nanoscales: optical nanocircuits inspired by metamaterials. Science **317**(5845), 1698–1702 (2007)

30. A. Alu, N. Engheta, Tuning the scattering response of optical nanoantennas with nanocircuit loads. Nat. Photonics **2**(5), 307–310 (2008)

31. N.H. Rafat, S.A. El-Naggar, S.I. Mostafa, Modeling of a wide band pass optical filter based on 1d ternary dielectric-metallic-dielectric photonic crystals. J. Opt. **13**(8), 085101 (2011)

32. P. Lalanne, J. Rodier, J. Hugonin, Surface plasmons of metallic surfaces perforated by nanohole arrays. J. Opt. A Pure Appl. Opt. **7**(8), 422 (2005)

33. Comsol BV, Comsol OY, Comsol multiphysics user's guide 1998–2010 comsol ab. (1998)

34. P.B. Johnson, R.W. Christy, Optical constants of the noble metals. Phys. Rev. B **6**, 4370–4379 (1972). https://doi.org/10.1103/PhysRevB.6.4370

35. F. Medina, F. Mesa, R. Marques, Extraordinary transmission through arrays of electrically small holes from a circuit theory perspective. IEEE Trans. Microw. Theory Tech. **56**(12), 3108–3120 (2008)

36. Q. Zhang, L. Bai, Z. Bai, P. Hu, C. Liu, Equivalent-nanocircuit-theory-based design to infrared broad band-stop filters. Opt. Express **23**(7), 8290–8297 (2015)

37. Q. Zhang, L. Bai, Z. Bai, P. Hu, C. Liu, Theoretical analysis and design of a near-infrared broadband absorber based on EC model. Opt. Express **23**(7), 8910–8917 (2015)

38. N. Marcuvitz, Waveguide Handbook, vol. 21. IET (1951)

39. S.A. Maier, Surface plasmon polaritons at metal/insulator interfaces. In: Plasmonics: Fundamentals and Applications, pp. 21–37. Springer, New York (2007)

40. J. Homola, *Surface Plasmon Resonance Based Sensors*, vol. 4 (Springer, Berlin, 2006)

41. C. Fabry, Theorie et applications d'une nouvelle methods de spectroscopie intereferentielle. Ann. Chim. Ser. **7**(16), 115–144 (1899)

42. N. Ismail, C.C. Kores, D. Geskus, M. Pollnau, Fabry-pérot resonator: spectral line shapes, generic and related airy distributions, linewidths, finesses, and performance at low or frequency-dependent reflectivity. Opt. Express **24**(15), 16366–16389 (2016)

43. Y. Xu, M. He, Design of multilayer frequency-selective surfaces by equivalent circuit method and basic building blocks. Int. J. Antennas Propag. **2019** (2019)

44. O. Luukkonen, C. Simovski, G. Granet, G. Goussetis, D. Lioubtchenko, A.V. Raisanen, S.A. Tretyakov, Simple and accurate analytical model of planar grids and high-impedance surfaces comprising metal strips or patches. IEEE Trans. Antennas Propag. **56**(6), 1624–1632 (2008)

45. H.A. Bethe, Theory of diffraction by small holes. Phys. Rev. **66**(7–8), 163 (1944)

46. A.E. Cetin, A.F. Coskun, B.C. Galarreta, M. Huang, D. Herman, A. Ozcan, H. Altug, Handheld high-throughput plasmonic biosensor using computational on-chip imaging. Light Sci. Appl. **3**(1), 122–122 (2014)

47. A. Hathat, Design of microstrip low-pass and band-pass filters using artificial neural networks. Algerian J. Signals Syst. **6**(3), 157–162 (2021)

48. P. Teo, K. Lee, C. Lee, Analysis and design of band-pass frequency-selective surfaces using the fem cad tool. Int. J. RF Microw. Comput. Aided Eng.: Co-sponsored by the Center for Advanced Manufacturing and Packaging of Microwave, Optical, and Digital Electronics (CAMPmode) at the University of Colorado at Boulder **14**(5), 391–397 (2004)

49. J. Lee, M. Seo, J. Sohn, Y. Ahn, D. Kim, S. Jeoung, C. Lienau, Q.-H. Park, Invisible plasmonic meta-materials through impedance matching to vacuum. Opt. Express **13**(26), 10681–10687 (2005)

50. S. Yin, X. Lu, N. Xu, S. Wang, E. Yiwen, X. Pan, X. Xu, H. Liu, L. Chen, W. Zhang et al., Spoof surface plasmon polaritons in terahertz transmission through subwavelength hole arrays analyzed by coupled oscillator model. Sci. Rep. **5**(1), 1–9 (2015)

51. B. Munkhbat, A.B. Yankovich, D.G. Baranov, R. Verre, E. Olsson, T.O. Shegai, Transition metal dichalcogenide metamaterials with atomic precision. Nat. Commun. **11**(1), 1–8 (2020)